Catalysis Science & Technology

PAPER

View Article Online
View Journal | View Issue

Cite this: *Catal. Sci. Technol.*, 2019, **9**, 1944

Accelerated charge transfer *via* a nickel tungstate modulated cadmium sulfide p–n heterojunction for photocatalytic hydrogen evolution

Yongke Zhang[abc] and Zhiliang Jin *[abc]

Received 29th December 2018,
Accepted 12th March 2019

DOI: 10.1039/c8cy02611d

rsc.li/catalysis

Improving the efficiency of charge separation is an important aspect in photocatalysis. With $NiWO_4$ modulation, the results of the Mott–Schottky test, short fluorescence lifetime (1.87 ns), faster electron transfer rate constant (K_{ET} = 2.82 × 10^8 s^{-1}), larger efficiency of electron injection (η_{inj} = 52.7%), high photocurrent response, smaller transfer resistance (R_{film} = 2785 Ω cm^2) and reaction resistance (R_{ct} = 1.74 Ω cm^2) showed that a new interface electric field was established and a more effective thermodynamic charge transfer path was formed. This evidence greatly supported the fact that the separation and transfer of space charges over CdS p–n were accelerated *via* $NiWO_4$ modulation. The [CdS/$NiWO_4$ (30%)] sample had the best H_2 production performance, namely, the maximum H_2 production in 5 hours was 757 μmol, which was 7.35 times higher than that of pure CdS nanorods. Moreover, a series of characterization results also showed that the $NiWO_4$ decorated CdS p–n heterojunction improved the efficiency of photo-generated charge separation and the SEM, XRD, TEM, EDX, XPS, UV-vis DRS, transient fluorescence, electro-chemistry *etc.* results were in good agreement with each other.

1. Introduction

The continuous depletion of fossil energy has caused mankind to face two major problems: energy shortage and environmental pollution.[1–3] These two issues have posed tremendous threats to the survival and development of human beings. Solar energy is a kind of sustainable clean energy.[4] Therefore, how to make good use of solar energy and improve the efficiency of energy conversion are the key to solving the energy crisis and environmental pollution problems. At present, photocatalytic technology is considered as an effective countermeasure, which can continuously convert low-density solar energy into chemical energy through photochemical reactions and has the advantages of low cost and environmental friendliness. It exhibits a very wide range of applications, such as in dye-sensitized solar cells,[5] photocatalytic degradation of pollutants,[6] photocatalytic cleavage of water to H_2,[7] photoelectrochemical cathodic protection[8] and photocatalytic reduction of CO_2.[9,10]

In 1972, Fujishima and Honda discovered that TiO_2 can decompose water into H_2 and O_2 under ultraviolet light,[11] and since then a large number of scientists have focused their attention on semiconductor photocatalysts such as ZnO,[12] CdS,[13,14] $BiVO_4$,[15,16] and Ag_3PO_4.[17] In addition to having an appropriate band gap energy level, an ideal semiconductor should have low cost, readily available materials, high stability, and be non-toxic, as well as exhibit efficient use of solar energy. However, few materials can satisfy the above conditions at the same time. For example, GaAs,[18] PbS,[19] and CdS are toxic, and they are prone to photo-corrosion and poor stability in aqueous solutions. ZnO is unstable in aqueous solution because it easily dissolves in water and can form $Zn(OH)_2$ on the surface of ZnO, thereby passivating the photocatalyst. The conduction band (CB) of Fe_2O_3,[20] SnO_2 (ref. 21) and WO_3 (ref. 22 and 23) is located in the lower part of the reversible hydrogen potential, which means that these materials need to be subjected to external bias to complete the hydrolysis reaction. However, photocatalytic technology faces many problems in practical applications, for example, how to increase the light absorption range of the photoelectric conversion material, the separation ability of the photoelectron–hole, and the stability of the photocatalytic catalytic performance.[24] Through extensive research, scientists have found that constructing an interface heterojunction system is an effective method to improve the separation efficiency of photogenerated electrons and holes.[25] The existence of these

[a] *School of Chemistry and Chemical Engineering, North Minzu University, Yinchuan 750021, P.R.China. E-mail: zl-jin@nun.edu.cn*
[b] *Ningxia Key Laboratory of Solar Chemical Conversion Technology, North Minzu University, Yinchuan 750021, P.R.China*
[c] *Key Laboratory for Chemical Engineering and Technology, State Ethnic Affairs Commission, North Minzu University, Yinchuan 750021, P.R.China*

electric fields can increase the efficiency of separation of photogenerated electrons and holes and improve the photocatalytic properties.[26]

CdS has become a research hotspot in the field of photocatalysis in recent years due to its characteristics of visible light response and high cost performance. It has also become a hotspot in the field of photoelectrocatalysis. It is the ideal bandgap of CdS and the suitable conduction band (CB) position that satisfy the thermodynamic and kinetic requirements of photocatalytic water splitting.[27] However, the lifetime of carriers generated by CdS itself is short and the redox reaction cannot be completed well. When the photogenerated holes are generated on the surface of CdS, if they cannot react with the surrounding sacrificial reagents or rapidly transfer to other substances, they will quickly oxidize CdS, resulting in rapid photo-corrosion[28] and rapid crystal structure collapse. The photocatalytic performance also deteriorates.

Therefore, in order to improve the stability and photocatalytic performance of the CdS photocatalyst, many researchers have extensively applied various nano-morphologies of CdS semiconductor-based materials to the field of photocatalysis: (1) CdS hollow spheres: Zhang J. L. and Xing M. Y. *et al.* reported the MnO_x@CdS/CoP hollow sphere photocatalyst, which was loaded with two cocatalysts (inside MnO_x and outside CoP) for enhancing photocatalytic H_2 evolution activities.[29] Han J. and Wang M. G. *et al.* prepared CdS/TiO_2 hollow sphere heterojunction photocatalysts to improve the photocatalytic activity.[30] (2) CdS nanorods: Li Z. Y. and Liang Q. *et al.* synthesized highly stable CdS@UIO-66-NH_2 core–shell nanorods for enhancing photocatalytic activity.[31] Zeng R. C. and Feng C. *et al.* prepared MoS_2 cluster modified CdS nanorods through a one-pot solvothermal method at lower temperature.[32] (3) CdS nanowires: Yu J. G. and Zhang J. Y. *et al.* prepared a CdS/g-C_3N_4 core/shell nanowire hybrid system by solvothermal and chemisorption methods.[28] (4) CdS quantum dots: Shi J. W. and Zou Y. J. *et al.* reported the study on CdS QD decorated WS_2/CN 2D/2D nanosheets for water splitting.[33] Wang X. C. and Zheng D. D. reported the integration of CdS quantum dots on hollow graphitic carbon nitride nanospheres for hydrogen evolution.[34] (5) CdS nanoparticles: Fang P. F. and Wang H. M. *et al.* reported the study on WO_3&WS_2 nanorods coupled with CdS nanoparticles for hydrogen evolution.[35] There are also some researchers who constructed a p–n type heterojunction[36] by forming a built-in electric field from the n-type semiconductor to the p-type CdS between the two semiconductors, thereby accelerating the separation of electrons and holes and effectively suppressing the recombination of the charges.

$NiWO_4$ has a characteristic wolframite structure with a monoclinic unit cell and space group,[37] suitable band gap energy (2.20 eV),[38] sufficient chemical and thermal stability, good quantum size effect, and excellent catalytic performance.[39] It is these properties that have attracted extensive attention and research in the field of photocatalysis, making it an ideal catalyst for photocatalytic decomposition of water to produce H_2. However, there are few reports on the use of the $NiWO_4$ photocatalyst for H_2 production from water splitting.

In this paper, we succeeded in constructing an efficient photocatalytic H_2 production system of CdS/$NiWO_4$. The first step is to synthesize CdS nanorods, and then load $NiWO_4$ to the surface of the CdS nanorods through a simple hydrothermal reaction. In the meantime, the p–n junction is formed between the p-type $NiWO_4$ (ref. 40) and n-type CdS, which accelerates the transfer of electrons and holes. As a result, the photocatalytic H_2 production rate is greatly improved.

2. Experimental section

2.1 Photocatalyst preparation

2.1.1 Preparation of CdS nanorods. A certain amount of $Cd(NO_3)_2{\cdot}6H_2O$ and NH_2CSNH_2 are dissolved in 50 ml of ethylenediamine, and magnetically stirred for 30 minutes. Subsequently, the solution is transferred to an 80 ml polytetrafluoroethylene autoclave and heated to 160 °C for 48 h. After the reaction is completed and cooled to room temperature, the sample is obtained by centrifugation. Then, the precipitate is washed with distilled water and ethanol three times and dried at 60 °C for 10 hours.

2.1.2 Preparation of CdS/$NiWO_4$ photocatalysts. CdS/$NiWO_4$ with different contents of $NiWO_4$ [m($NiWO_4$)/m(CdS) × 100% = 5, 10, 30, 50 and 70] are prepared by a solvothermal method. Taking the preparation of the [CdS/$NiWO_4$ (50%)] catalyst as an example, in a typical synthesis of the composite catalysts, firstly, 200 mg of the above-prepared CdS nanorods are added to a 100 ml beaker containing 60 ml of DI water and sonicated for 20 minutes. Soon afterwards, 77.46 mg of $NiCl_2{\cdot}6H_2O$ and 107.5 mg $Na_2WO_4{\cdot}6H_2O$ are added to the above solution. After magnetic stirring for 30 minutes, the above solution is transferred to a 100 mL autoclave and heated to 130 °C for 12 h. Finally, after cooling down to room temperature, the sample is obtained by centrifugation, washing and drying. The other catalysts with different percentages $NiWO_4$ are also prepared in the same way. We use [CdS/$NiWO_4$ (x%)] (x = 5, 10, 30, 50, 70) to represent these samples.

2.2 Photocatalytic H_2 measurements

We use 62 ml reaction bottles and a PCX50A Discover (Perfectlight, Beijing) for photocatalytic H_2 production measurements. The specific steps are as follows: first of all, 20 mg of the sample, 30 ml of 10 vol% lactic acid and a magnetic stir bar are added to the reaction bottle. Then, after stirring for 5 minutes, we put the reaction bottle into the ultrasonic cleaner for sonication for 10 minutes. Subsequently, the system is ventilated with N_2 for about 30 min to remove O_2. Ultimately, we place the reactor on the multi-channel reaction system and extract 0.5 ml of gas to analyze through gas chromatography (Tianmei GC7900, TCD, 13× column, N_2 as the carrier). We use the external standard method to calculate the amount of H_2 produced.

Next, we test the apparent quantum efficiency (AQE) of the [CdS/$NiWO_4$ (30%)] composite catalyst. The specific steps

are as follows: 20 mg of the [CdS/$NiWO_4$ (30%)] catalyst is placed in a 62 ml quartz reaction flask containing 30 ml of 10% lactic acid solution, then the oxygen in the bottle is replaced with N_2 for 10 minutes and ultrasonic treatment is conducted for 10 minutes. A 300 W Xe lamp light source (CEL-HXF300) with 400, 420, 450, 475, 500, 520, 550 and 600 nm band pass filters is used as the light source to irradiate the reaction solution for 1 h separately. A PL-MW200 photoradiometer (Perfect Light) is used to measure the photon flux of the incident light. Based on eqn (1), the AQE at different wavelengths is calculated.

$$\mathrm{AQE} = \frac{2 \times \text{the number of evolved hydrogen molecules}}{\text{the number of incident photos}} \times 100\% \quad (1)$$

2.3 Photoelectrochemical measurements

Photoelectrochemistry experiments are conducted on an electrochemical workstation (VersaSTAT4-400, AMETEK) using a homemade standard three-electrode cell, whose reference electrode, counter electrode and working electrode are respectively a saturated calomel electrode (SCE), Pt electrode and FTO (1 × 2 cm^2) drop-coating homogeneous catalyst. The electrolyte is a Na_2SO_4 aqueous solution (0.2 mol L^{-1}). A 300 W xenon lamp with a cut-off filter of 420 nm is used as the light source. The Mott–Schottky plot is recorded at 5 kHz frequency in the dark. The potential ranges from −1.5 to 2.0 V (*vs.* SCE).

2.4 Characterization

The crystalline structure, element composition and UV-vis diffuse reflectance spectra are respectively measured using an X-ray diffractometer (XRD, Rigaku RINT-2000), X-ray photoelectron spectroscope (XPS, ESCALAB 250Xi) and UV-2550 (Shimadzu) spectrometer ($BaSO_4$ as the reference). The images of sample morphology are obtained using a field-emission scanning electron microscope (FESEM, JSM-6701F) and a transmission electron microscope (TEM, Tecnai G2-TF30). The nitrogen adsorption–desorption isotherms are measured at 77 K with an ASAP 2020 M instrument and analyzed using the Brunauer–Emmett–Teller (BET) equation. The pore size distribution plots are obtained by the Barrett–Joyner–Halenda (BJH) model. The photoluminescence (PL) emission spectra and time-resolved PL (TRPL) spectra are detected using a FluoroMAX-4 spectrometer (Horiba, France).

3. Results and discussion

3.1 XRD, SEM, and TEM analysis

3.1.1 XRD analysis. Fig. 1 shows the XRD patterns of the samples. In Fig. 1(A), in order to more intuitively observe and analyze the phase and crystallinity of the samples, we select the [CdS/$NiWO_4$ (70%)] sample for analysis. It can be seen that in the characteristic peaks of the [CdS/$NiWO_4$ (70%)] sample, not only the characteristic peaks of CdS but also the characteristic peaks of $NiWO_4$ can be indexed. Through further observation, it can be observed that there are seven main sharp peaks at 2Θ = 24.85, 26.48, 28.24, 36.58, 43.78, 47.77 and 51.88°, matching well with the corresponding lattice faces of (100), (330), (101), (102), (110), (103) and (112), respectively (CdS with a space group of *P*63*mc* (no. 186), JCPDS no. 65-3414),[42,43] and that there are four peaks located at 19.29, 31.11, 36.58 and 54.60°, which are consistent with the monoclinic $NiWO_4$ phase (JCPDS no. 15-0755) with a space group of *P*2/*c* (no. 13) and correspond to the (100), (−111), (002) and (−202) planes, respectively. The three strong peaks of CdS and $NiWO_4$ are obvious, and there are basically no other impurity peaks. Fig. 1(B) shows the XRD patterns of [CdS/$NiWO_4$ (*x*%)] (*x* = 5, 10, 30, 50, 70). When the content of $NiWO_4$ is gradually increased, the intensity of the characteristic peak of $NiWO_4$ in the XRD pattern is also gradually enhanced, especially that of the 31.11° characteristic peak, demonstrating that the content of $NiWO_4$ loaded on the CdS/$NiWO_4$ is also gradually increasing.

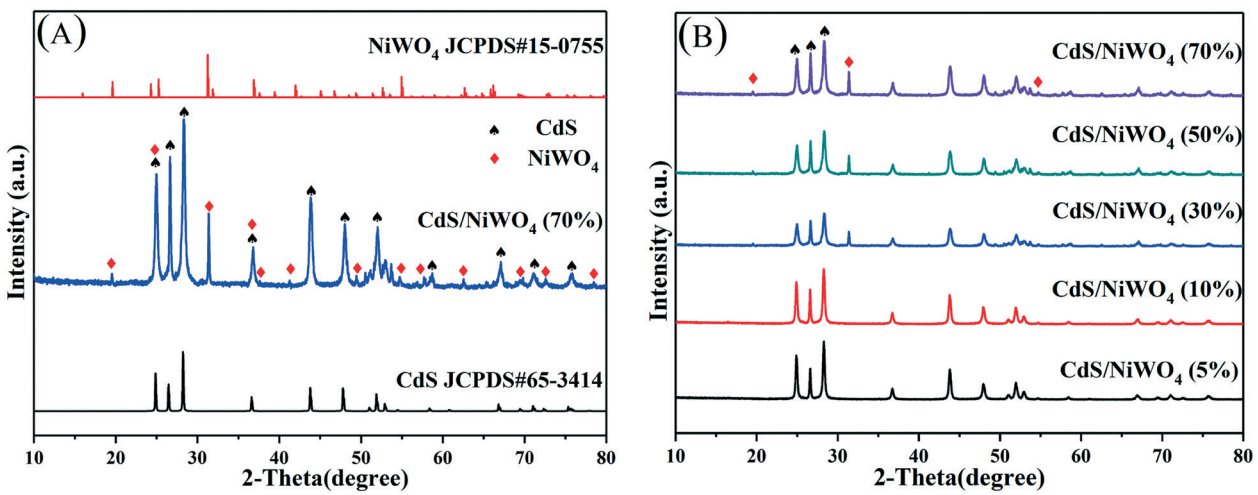

Fig. 1 The XRD patterns of (A) CdS/$NiWO_4$ (70%) and JCPDS of CdS and $NiWO_4$; (B) the XRD patterns of [CdS/$NiWO_4$ (*x*%)] (*x* = 5, 10, 30, 50, 70).

3.1.2 SEM analysis. The morphology of CdS nanorods and [CdS/$NiWO_4$ (30%)] is examined by SEM, the results of which are utilized to offer more intuitive information about the space shape, size, sample distribution of samples and so on. Fig. 2(A) and (B) show the SEM photographs of CdS nanorods at low magnification and high magnification, respectively. It can be clearly seen that the CdS nanorods are uniformly dispersed, with a size distribution of approximately 1 μm and a relatively smooth surface. Fig. 2(C) and (D) show the SEM images of [CdS/$NiWO_4$ (30%)] at low magnification and high magnification, respectively. It can be found that the comparatively smooth surface of CdS nanorods becomes rough, and that there are many plate-like structures adhering to the surface of the CdS nanorods, manifesting that $NiWO_4$ successfully attached to the surface of CdS nanorods, which can be verified by further TEM characterization.

3.1.3 TEM analysis. TEM and HRTEM characterizations of the samples are of great importance in increasing the understanding of the internal structure and the morphology after the loading of $NiWO_4$. In Fig. 3(A), we can further see that the CdS nanorods are uniformly dispersed, and the surface is relatively smooth, which is consistent with the XRD and the SEM results. On further observation of the HRTEM image in Fig. 3(B), the lattice spacing in the middle of two adjacent lattice planes is about 0.336 nm,[27] which matches with the (002) lattice plane of CdS. Fig. 3(C and D) show the TEM images of [CdS/$NiWO_4$ (30%)] at different magnifications from low to high. It is very clear that there is a sheet-like structure attached to the surface of the CdS nanorod. This is in agreement with the SEM image in Fig. 2(D). Further analysis of the HRTEM image in Fig. 3(E) shows that the lattice spacings in the middle of two adjacent lattice planes are about 0.336 and 0.245 nm,[29] which matched the (002) lattice plane of CdS (ref. 27) and the (002) lattice plane of the monoclinic $NiWO_4$,[43] respectively. Fig. 3(F) shows the energy dispersive X-ray spectroscopy (EDX) spectrum of [CdS/$NiWO_4$ (30%)] and the results demonstrate the presence of S, Cd, Ni, W and O elements.

3.2 XPS, BET, and UV-vis DRS analysis

3.2.1 XPS analysis. In order to further understand the element composition of the sample and the valence of each element, XPS studies on as-prepared [CdS/$NiWO_4$ (30%)] are carried out so that we can obtain deeper insights. From the survey spectrum (Fig. 4(A)), we can find that the composite catalyst mainly consists of S, Cd, Ni, W and O elements. It can be seen that the S 2p spectrum (Fig. 4(B)) can be deconvoluted into two peaks including 161.76 eV for S $2p_{3/2}$ and 162.94 eV for S $2p_{1/2}$,[44] and that the Cd 3d spectrum (Fig. 4(C)) can be resolved into two peaks located at 412.05 and 405.26 eV, which are ascribed to Cd $3d_{5/2}$ and Cd $3d_{3/2}$, respectively.[45] In the Ni 2p spectrum in Fig. 4(D), it can be seen that there are six distinct characteristic peaks in the Ni

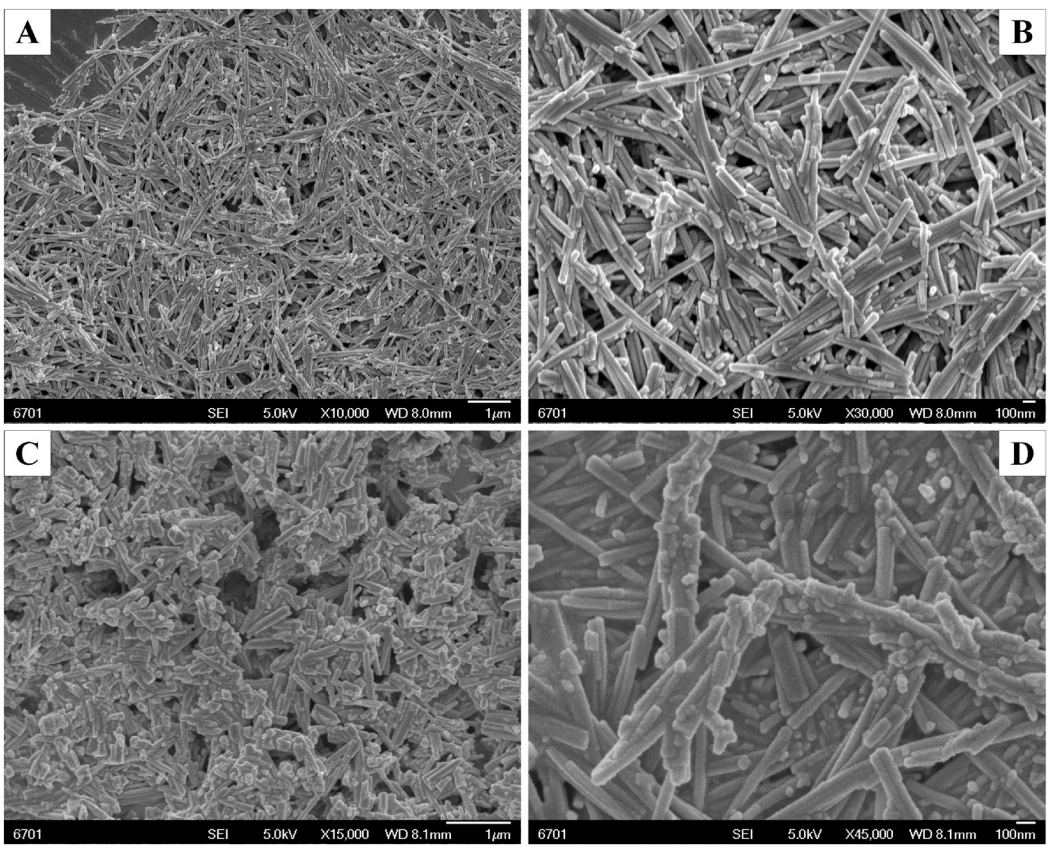

Fig. 2 SEM images: (A and B) CdS nanorods; (C and D) CdS/$NiWO_4$ (30%).

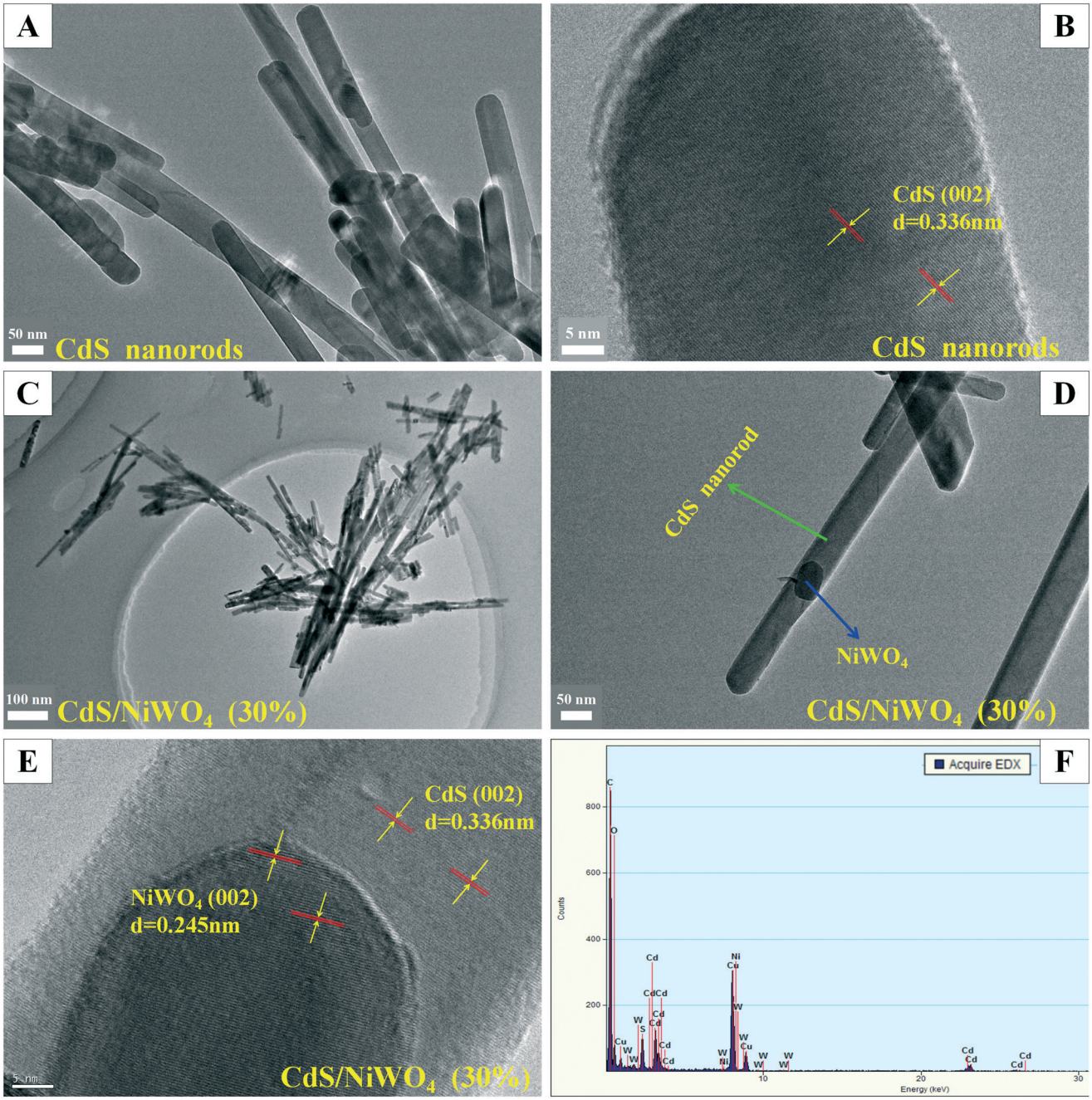

Fig. 3 (A and B) TEM and HRTEM images of CdS nanorods, (C–E) TEM and HRTEM images of [CdS/$NiWO_4$ (30%)] and (F) EDX spectrum of [CdS/$NiWO_4$ (30%)].

spectrum, which belong to the Ni $2p_{3/2}$ and Ni $2p_{1/2}$ area, respectively. Further observation of the Ni 2p spectrum reveals that there are three distinct characteristic binding energy peaks located in the Ni $2p_{3/2}$ region. The three peaks are located at 852.3, 855.9 and 861.3 eV, which matched the $Ni^{\delta+}$ in $NiWO_4$, the Ni^{2+} species oxidation state and the satellite peak, respectively. Similarly, in the Ni $2p_{1/2}$ region, three peaks are located at 869.2, 874.2 and 880.1 eV, which originated from the $Ni^{\delta+}$ in $NiWO_4$, the Ni^{2+} species oxidation state and the satellite peak.[46] In Fig. 4(E), the W 4f spectrum can be deconvoluted into well-resolved spin orbit split doublet peaks at 35.7 and 37.8 eV,[37,47] which correspond to W $4f_{7/2}$ at 35.7 eV and W $4f_{5/2}$ at 37.8 eV, with a spin energy separation of 2.1 eV which is consistent with the previous report for W^{6+}.[37] Besides, both the W $4f_{7/2}$ peak at 35.7 eV and the Ni $2p_{3/2}$ peak at 855.9 eV demonstrate the formation of a Ni tungstate binary metal oxide. From the O 1s spectrum in Fig. 4(F), we can see that there is a major peak located at 531.9 eV,[47] which is ascribed to the lattice oxygen in the $NiWO_4$ phase indicating the presence of $NiWO_4$.[47]

3.2.2 BET analysis. The physical adsorption properties of the samples are of great importance not only for the

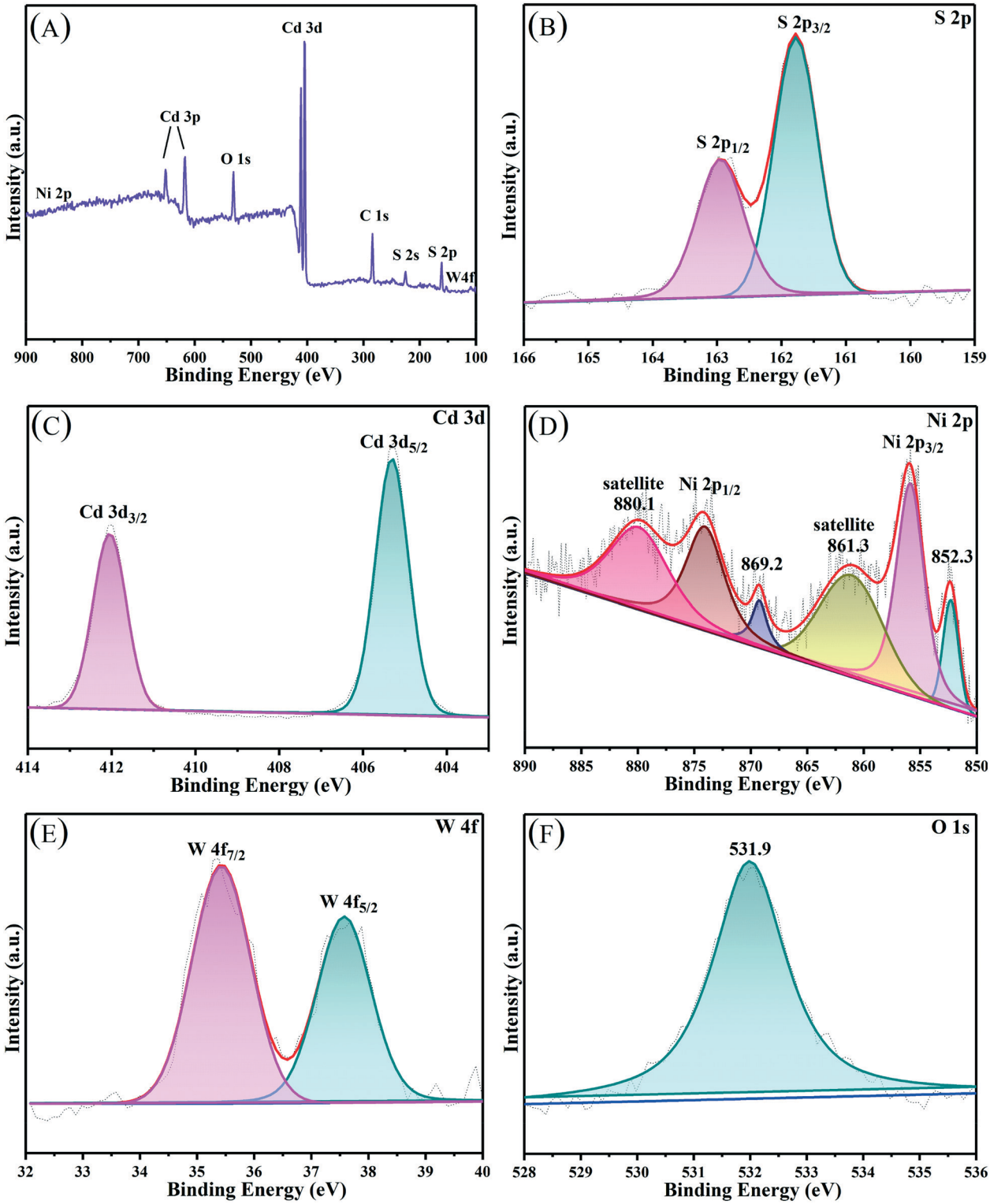

Fig. 4 XPS patterns of the [CdS/$NiWO_4$ (30%)] sample. (A) Survey, (B) S 2p, (C) Cd 3d, (D) Ni 2p, (E) W 4f and (F) O 1s scan spectra.

realization of improved sample performance, but also for affecting the catalytic reaction. The adsorption and desorption properties of the samples rely on their specific surface area, pore volume and pore size. In order to obtain the nitrogen adsorption and desorption isothermal curves, pore size distribution curves and physical adsorption desorption performance parameters of the samples, we utilize the ASAP 2020 M instrument at 77 K to carry out the experiment, whose results are shown in Fig. 5(A and B) and Table 1. From Fig. 5(A), we can observe that the adsorption/desorption

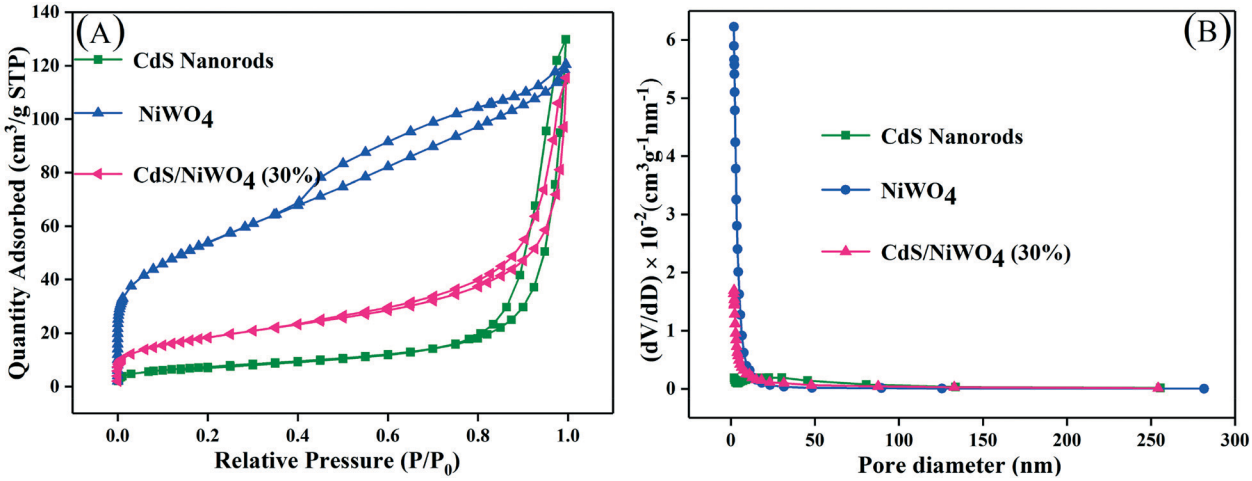

Fig. 5 (A) The N_2 adsorption–desorption isotherms and (B) corresponding pore size distribution curves.

Table 1 The physical adsorption performance parameters

Samples	S_{BET}[a] ($m^2\ g^{-1}$)	Pore volume[b] ($cm^3\ g^{-1}$)	Average pore size[b] (nm)
CdS	27	0.20	24.0
$NiWO_4$	190	0.18	4.1
$CdS/NiWO_4$ (30%)	66	0.18	11.1

[a] Obtained from the BET method. [b] Relative pressure (P/P_0) was 0.99.

curves of CdS nanorods, $NiWO_4$ and [$CdS/NiWO_4$ (30%)] belong to the type IV isotherm, whose hysteresis loop is of the H3 type. We can draw a conclusion from Fig. 5(B) that the three materials are mesoporous materials on the basis of the pore size distribution curve and the average pore size.

On further analysis of Table 1, we can see that the specific surface area of pure CdS nanorods and $NiWO_4$ is 27 and 190 $m^2\ g^{-1}$, respectively. At the same time, we can see that the pure CdS nanorods have a larger average pore size, reaching 24.0 nm, and that $NiWO_4$ has a minimum average pore size of 4.1 nm. When 30% of $NiWO_4$ is loaded onto the surface of CdS nanorods, the specific surface area of the composite catalyst [$CdS/NiWO_4$ (30%)] is between those of CdS nanorods and $NiWO_4$, which indicates that $NiWO_4$ has been successfully loaded onto the surface of CdS nanorods, which is beneficial to the photocatalytic reactions.

3.2.3 UV-vis DRS analysis. Light absorption performance is of great importance in influencing the H_2 production activity. Therefore, we use a diffuse reflectance spectrometer to test the photoresponse behavior of the samples. Fig. 6(A) shows

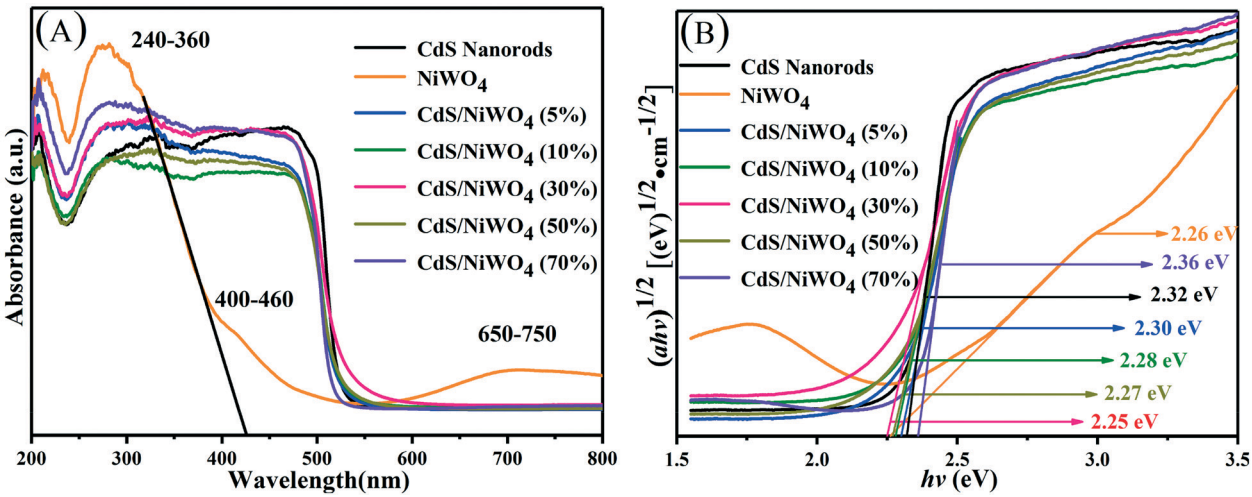

Fig. 6 (A) The UV-vis diffuse reflectance spectra; (B) the plot of transformed Kubelka–Munk function *vs.* the energy.

that the pure CdS nanorods have prominent optical absorption in the UV and visible light regions exhibiting an absorption edge located at 525 nm, and that $NiWO_4$ has outstanding optical absorption in the UV and visible light regions. In addition, three absorption bands (240–360 nm, 400–460 nm and 650–750 nm) of $NiWO_4$ can be clearly seen,[48] which are

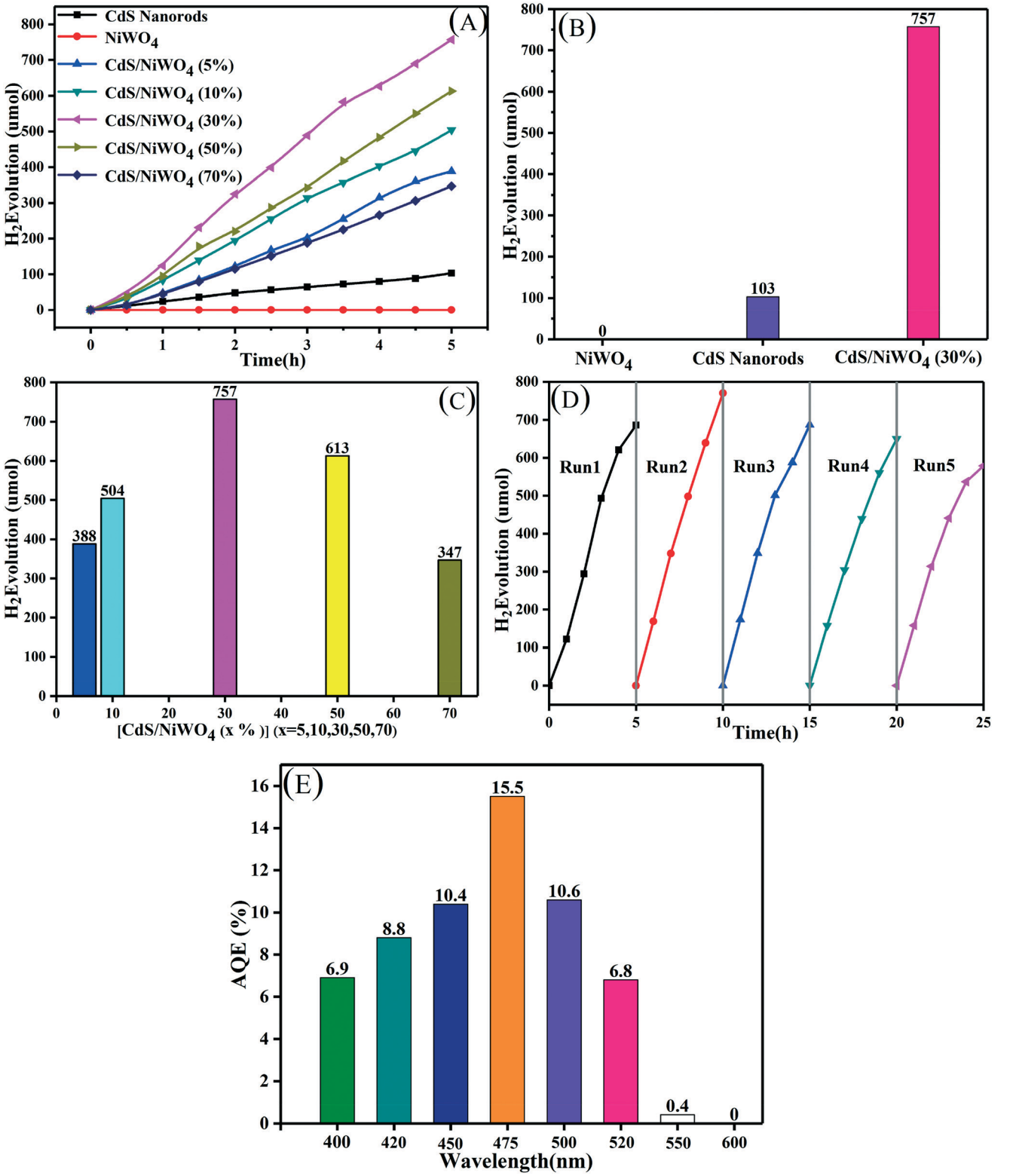

Fig. 7 (A–C) The H_2 production activity curves of CdS nanorods, $NiWO_4$ and [$CdS/NiWO_4$ (*x*%)] (*x* = 5, 10, 30, 50, 70) in 30 ml 10% lactic acid solution; (D) stability test on the [$CdS/NiWO_4$ (30%)] sample; (E) the AQE of the [$CdS/NiWO_4$ (30%)] sample in 30 ml 10% lactic acid solution.

caused by the oxidation state of the cations, in agreement with those reported in the literature by M. M. Mohamed and assigned to the $NiWO_4$ formation.[48] For [CdS/$NiWO_4$ (x%)] (x = 5, 10, 30, 50, 70), on the one hand, the absorption edge becomes larger, that is to say, their absorption edge has a tendency to red shift;[42] on the other hand, the light absorption intensity is enhanced in the wavelength range from 600 to 800 nm.

In order to obtain the energy band gap (E_g) of the samples, we draw the Tauc graph from the UV-vis diffuse reflectance spectra. The E_g is estimated by the function (eqn (2)):

$$\begin{aligned} &(\alpha h\nu)^{1/2} = A(h\nu - E_g) \\ &\alpha - \text{the absorption coefficient;} \\ &h - \text{Plank's constant (incident photon energy);} \\ &\nu - \text{the frequency of radiation;} \\ &A - \text{a constant;} \end{aligned} \tag{2}$$

From CdS nanorods to [CdS/$NiWO_4$ (70%)], the E_g values are estimated to be 2.32, 2.26, 2.30, 2.28, 2.27, 2.25 and 2.36 eV, respectively. It may be the different colors of the samples and different percentages of $NiWO_4$ that lead to different light absorption intensities. The light absorption intensity of the photocatalyst increases with the increase of the percentage of $NiWO_4$. Nevertheless, excessive loading of $NiWO_4$ on the surface of CdS nanorods will prevent CdS from absorbing visible light,[41] thereby reducing the photocatalytic H_2 production activity.

3.3 Photocatalytic H_2 evolution performance

In order to test the photocatalytic H_2 production performance and the stability of the samples, they are tested in a 10% lactic acid solution, and the results are shown in Fig. 7. We break down Fig. 7(A) into Fig. 7(B) and (C) so that we can study the H_2 production performance of CdS nanorods and $NiWO_4$ and the effect of different percentages of $NiWO_4$ on the H_2 production performance. From Fig. 7(B), we can see that pure $NiWO_4$ did not produce H_2 within 5 h, which means that pure $NiWO_4$ has no photocatalytic H_2 production activity. The H_2 production of CdS nanorods for 5 hours is the smallest, reaching 103 μmol, due to the rapid recombination of photogenerated electrons and holes. When 30% $NiWO_4$ is deposited on the surface of CdS nanorods, by testing, the H_2 production amount reaches the maximum of 757 μmol, which is 7.35 times higher than that of CdS nanorods.

In order to study the effect of the content of $NiWO_4$ on the H_2 production activity, we test the H_2 production performance of the different percentages of the composite catalyst [CdS/$NiWO_4$ (x%)] (x = 5, 10, 30, 50, 70) prepared above, and the results are shown in Fig. 7(C). The hydrogen yield of the composite catalysts exhibits the shape of an arch bridge, that is, as the percentage content of $NiWO_4$ increases, the amount of H_2 production also increases. The amount of H_2 production reaches the maximum (757 μmol, 5 h) when the percentage content of $NiWO_4$ is 30%. Subsequently, when the percentage of $NiWO_4$ is continuously increased, the amount of hydrogen production begins to decrease gradually. This may be attributed to the phenomenon that superfluous $NiWO_4$ not only can absorb more visible light by itself, but also can occupy some active sites of CdS nanorods, thus inhibiting the H_2 production activity.[41]

Further, in order to evaluate the stability of catalyst activity, the [CdS/$NiWO_4$ (30%)] sample is selected to be tested in a 10 vol% lactic acid solution. We perform a total of 5 cycles of 5 hours each. When the end of each cycle is ended, the reaction system is replaced with N_2 to remove hydrogen from the last cycle. In Fig. 7(D), we can see that the total amount of H_2 in each cycle is almost equal and the slight decrease in hydrogen production in the fifth cycle may be due to lactic acid consumption, which indicates that the catalyst activity is relatively stable. Further, we test the AQE of the [CdS/$NiWO_4$ (30%)] composite catalyst at different wavelengths. The results are shown in Fig. 7(E): it can be seen that as the monochromatic wavelength increases, the AQE also increases, and the AQE reaches 15.5% when the monochromatic wavelength is 475 nm. When a larger monochromatic wavelength is used, the AQE begins to decrease; when the monochromatic wavelength is up to 550 nm, the AQE is only 0.4%, indicating that the catalyst produces little H_2 at this wavelength. When the wavelength of monochromatic light is 600 nm, the AQE is 0, indicating that the wavelength cannot excite the [CdS/$NiWO_4$ (30%)] composite catalyst.

We can draw conclusions from the above analysis results: the p–n type heterojunction between CdS nanorods and $NiWO_4$ is successfully formed; under the internal electric field and potential difference, the electron and hole migration speeds are accelerated, thus improving the H_2 production performance of the composite catalyst.

3.4 Separation mechanism of charge transfer

3.4.1 PL spectra and TRPL spectra. The separation and transfer of charge and the lifetime of electrons and holes are of great importance in elucidating the possible charge separation and transfer mechanisms. Therefore, photoluminescence experiments and fluorescence lifetime decay experiments are carried out. The results are shown in Fig. 8 and Table 2. Fig. 8(A and C) show the photoluminescence (PL) spectra of CdS nanorods, [CdS/$NiWO_4$ (5%)], [CdS/$NiWO_4$ (30%)], [CdS/$NiWO_4$ (70%)] and $NiWO_4$. In Fig. 8(A), the PL spectra of all the samples present a parabolic shape with different intensities. Their emission wavelength center is approximately 520 nm while the excitation wavelength is 380 nm. In Fig. 8(C), when the excitation wavelength is 290 nm, the emission wavelength of $NiWO_4$ nanoparticles ranges from 300 to 550 nm, which is similar to other wolframite compounds.[32] It is the WO_6^{6-} anion along with some defects in the crystal structure that determines the fluorescence emission peak of $NiWO_4$.[32] The emission peak at 350 nm is from the band gap transition. The doublet peaks appear at 382 and 395 nm, which are due to either the quantum size[49] or to the interference between

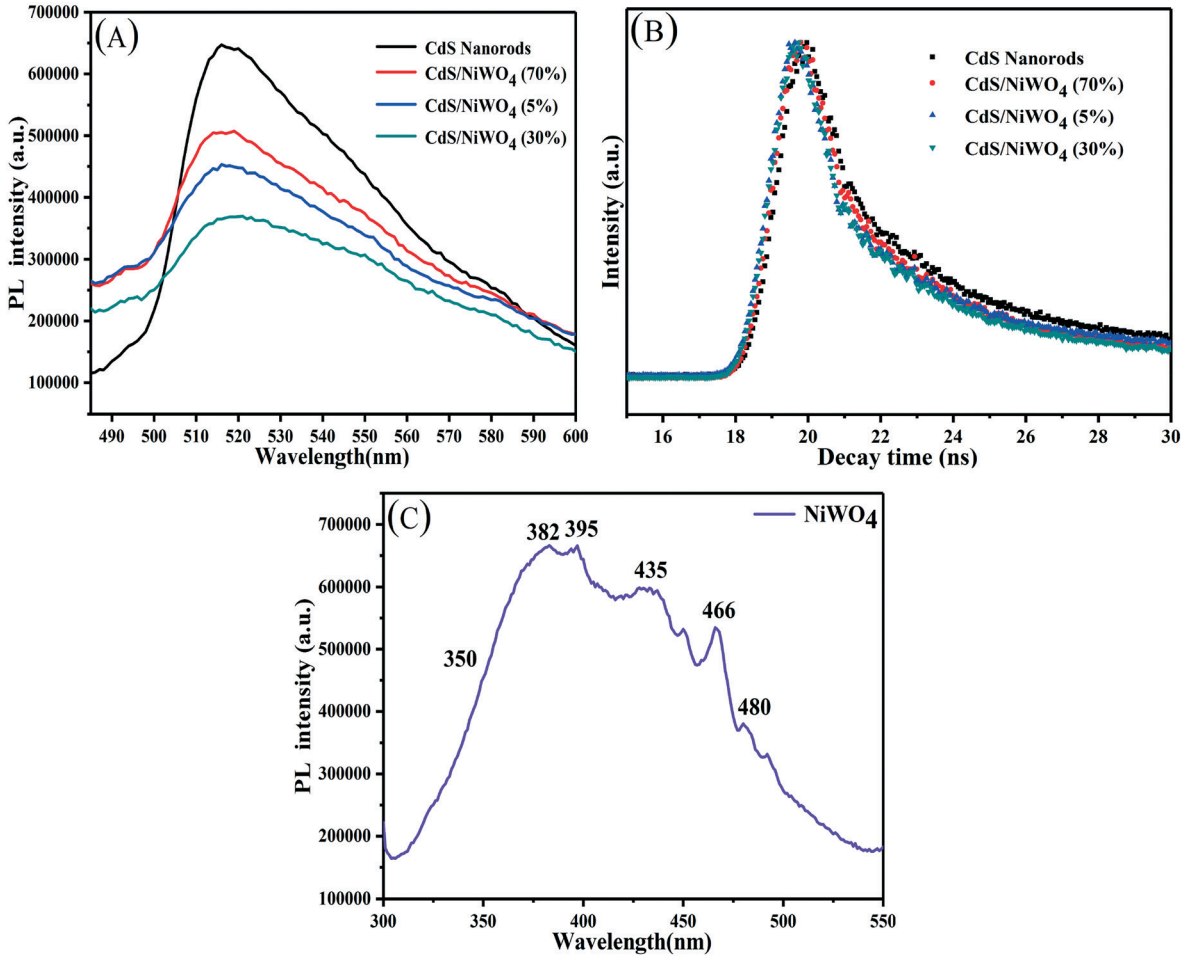

Fig. 8 (A and C) The PL spectra and (B) the time-resolved photoluminescence (TRPL) spectra.

Table 2 The exponential curve fitted parameters of emission decay for the samples

Samples	T_1 [ns]	A_1 [%]	T_2 [ns]	A_2 [%]	T_3 [ns]	A_3 [%]	χ^2	τ_{ave} [ns]	K_{ET} [10^9 s^{-1}]	$\eta_{(inj)}$ [%]
CdS	5.60	22.11	0.69	17.58	160.4	60.31	1.89	3.96	—	—
$CdS/NiWO_4$ (70%)	5.32	22.67	0.59	17.75	150.8	59.58	1.90	2.90	0.092	26.7
$CdS/NiWO_4$ (5%)	5.24	22.96	0.55	18.56	149.5	58.48	1.91	2.58	0.135	34.8
$CdS/NiWO_4$ (30%)	4.44	25.90	0.41	19.54	101.7	54.65	2.02	1.87	0.282	52.7

the luminescence band of the WO_6 groups and the absorption band of the NiO_6 groups.[50] The other obvious emission peaks appear at 435, 466 and 480 nm, which are related to the intensive transition from the ground state $^3A_{2g}$ to the excited state $^3T_1$ of Ni^{2+} ($3d^8$) ions in a distorted octahedral coordination[32] or due to recombination of e–h pairs localized at oxygen-atom-deficient tungstate ions.[51] Compared with that of CdS nanorods, the emission peak fluorescence intensity of $NiWO_4$ is the strongest, which indicates that it has the highest degree of combination of electrons and holes. When different amounts of $NiWO_4$ are adhered to the surface of CdS nanorods, the fluorescence intensity of the emission peaks is quenched to varying degrees. As the percentage of $NiWO_4$ increases, the emission peak intensity first decreases and then increases, and the emission peak of [$CdS/NiWO_4$ (30%)] is the weakest and quenched to the maximum extent. Based on the above results, we can further draw the conclusion: the p–n junction and an internal electric field between $NiWO_4$ and CdS are formed. It is the internal electric field that accelerates the rapid separation and transfer of electrons and holes, thereby effectively enhancing the photocatalytic activity of H_2 production.

What's more, time-resolved photoluminescence (TRPL) is a promising approach to observe the kinetics of electron transfer and further study the separation and transfer of photogenerated electrons and holes. In Fig. 8(B), the decay curves of the samples are fitted by a triexponential decay function (eqn (3)).[27] The composite catalysts demonstrate a faster TRPL decay compared with CdS nanorods, which indicates efficient charge separation.

$$I(t) = \sum_{i=1,2,3} B_i \exp(-t/\tau_i)$$
I – the normalised emission intensity;
t – the time after the pulsed laser excitation; (3)
B_i – the amplitude (pre-exponential factor);
τ_i – the TPRL decay time;

From the fitting parameters in Table 2, it can be seen that the short lifetime (T_1, T_2) and long lifetime (T_3) gradually reduce. We use eqn (4)[27] to calculate the average lifetime (τ_{ave}) so that we can better understand the effect of $NiWO_4$ content on the decay life of the composite catalysts.

$$\langle\tau\rangle = \sum_{i=1,2,3} B_i\tau_i^2 \Big/ \sum_{i=1,2,3} B_i\tau_i$$
$\langle\tau\rangle$ – the average lifetime;
B_i – the amplitude (pre-exponential factor); (4)
τ_i – the TPRL decay time;

The average lifetime of CdS nanorods, [CdS/$NiWO_4$ (70%)], [CdS/$NiWO_4$ (5%)] and [CdS/$NiWO_4$ (30%)] is 3.96, 2.90, 2.58 and 1.87 ns, respectively. Generally speaking, the shorter the electron lifetime, the faster the electron transfer rate. The above results reflect the transfer of electrons from CdS nanorods to $NiWO_4$ in a relatively short period of time. Using the average lifetime of the samples, we further calculate the electron transfer rate constant (K_{ET})[52] and the electron injection efficiency (η_{inj})[53,54] using eqn (5) and (6) respectively:

$$K_{ET} = \frac{1}{\tau_{ave}(\text{sample})} - \frac{1}{\tau_{ave}(\text{CdS})} \quad (5)$$

$$\eta_{inj} = 1 - \frac{\tau_{ave}(\text{sample})}{\tau_{ave}(\text{CdS})} \quad (6)$$

Based on the above formula, from [CdS/$NiWO_4$ (5%)] to [CdS/$NiWO_4$ (30%)], the electron transfer rate constant (K_{ET}) and electron injection efficiency (η_{inj}) are calculated to be 0.092 × 10^9, 0.135 × 10^9, 0.282 × 10^9 s^{-1} and 31.4, 36.9 and 44.7%, respectively. Therefore, the above results further prove that the p–n type heterojunction between $NiWO_4$ and CdS is successfully formed. It's the p–n heterojunction that makes the electrons rapidly transfer from the conduction band (CB) of $NiWO_4$ to that of CdS in a relatively short time, further participating in the process of H_2 production.

3.4.2 Photoelectrochemical (*i–t* and EIS) analysis. It is well known that the photoelectric properties of catalysts are also important factors affecting the separation and transfer of electrons and holes. Photocurrent density–time experiments (*i–t*) and AC impedance experiments (EIS) were conducted to determine the photoelectric properties of the samples. To this end, we carry out the above experiments in 0.2 M Na_2SO_4 aqueous solution.

Fig. 9(A) shows the photocurrent density–time curve of CdS nanorods, $NiWO_4$ and [CdS/$NiWO_4$ (x%)] (x = 5, 10, 30, 50, 70). In order to observe the photocurrent response of $NiWO_4$ clearly and intuitively, we deconvolute the photocurrent response of $NiWO_4$ in Fig. 9(A), and the result is shown in Fig. 9(B). It can be seen that $NiWO_4$ nanoparticles have the lowest photocurrent density, and that the photocurrent density of pure CdS nanorods is improved to some extent compared to that of $NiWO_4$ nanoparticles. Further, considering Fig. 9(A and B), it can be concluded that the photocurrent density of the pure CdS nanorods is 16.24 times higher than that of the $NiWO_4$ nanoparticles. When $NiWO_4$ is loaded onto the CdS nanorods, the photocurrent density of the composite catalyst is improved. After 5 cycles of light on/off, the photocurrent density of the composite catalyst showed a downward trend, which may be due to the existence of certain photo-corrosion of CdS under light conditions in 0.2 M Na_2SO_4 aqueous solution. On further observation, it can be found that with the increase of $NiWO_4$ content, the photocurrent density of the composite catalyst also increases; when the loading of $NiWO_4$ reaches 30%, the photocurrent density is the largest; when the content of $NiWO_4$ continues to increase, the photocurrent density begins to decrease. The photocurrent density results of the above samples correspond to the photocatalytic hydrogen production activity shown in Fig. 7(A).

The AC impedance spectroscopy (EIS) technique can be used to qualitatively study the migration ability of electrons in a photoanode film and the electron exchange capability between the photoanode and the electrolyte interface. Fig. 9(C) shows the AC impedance spectrum of CdS nanorod, $NiWO_4$ and [CdS/$NiWO_4$ (x%)] (x = 5, 10, 30, 50, 70) photoelectrodes in dark state. The smaller the arc radius, the smaller the interface charge transfer resistance. The arc radius of [CdS/$NiWO_4$ (30%)] is the smallest, which means that the conductivity of the [CdS/$NiWO_4$ (30%)] photoelectrode is outstanding. The illustration shows the equivalent circuit diagram. The solution resistance (R_{sol}), the transfer resistance of photogenerated electrons in the photoelectrode material (R_{film}) and the interfacial reaction resistance (R_{ct}) together constitute the AC impedance value of the photoelectrode. In addition, Q represents the original phase angle; C represents the interface capacitance. The fitted EIS data of CdS and [CdS/$NiWO_4$ (30%)] are shown in Table 3. It can be seen from the fitting results in Table 3 that the R_{film} of the CdS nanorods modified by $NiWO_4$ decreased from 2.77 × 10^4 Ω cm^2 to 2785 Ω cm^2, which is about 10 times lower; the R_{ct} decreased from 11.43 Ω cm^2 to 1.74 Ω cm^2; C is increased from 9.43 × 10^{-5} μF cm^{-2} to 3.2 × 10^{-3} μF cm^{-2}, indicating that the surface state density of the $NiWO_4$ modified CdS nanorods has increased significantly. The above results indicate that the interface electric

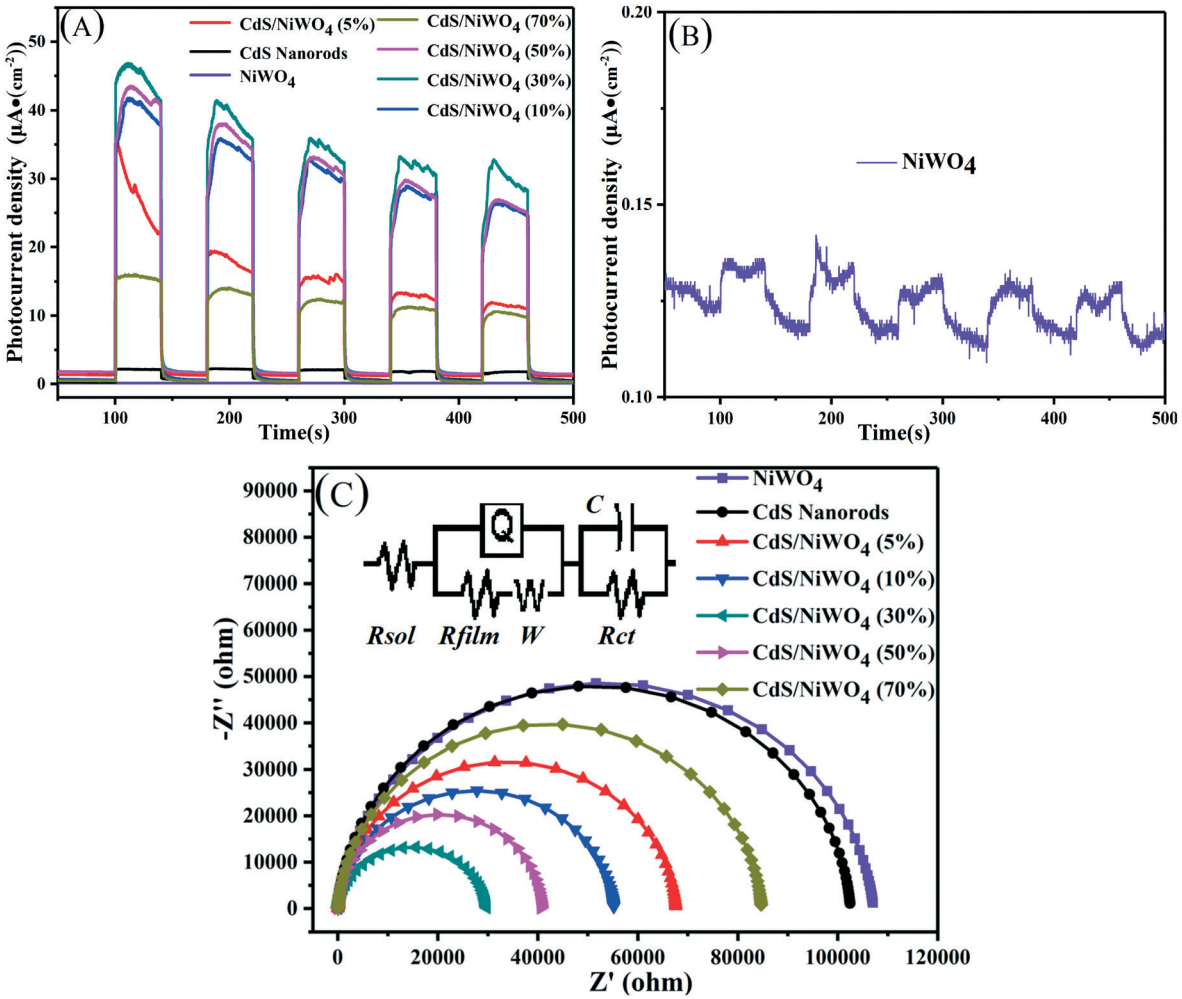

Fig. 9 (A) Transient photocurrent responses; (B) transient photocurrent response of $NiWO_4$; (C) electrochemical impedance spectroscopy (EIS) (0.2 M Na_2SO_4, $\lambda \geq 420$ nm).

Table 3 The parameters of potentiostatic EIS fitted by ZsimpWin

Samples	R_{sol} [Ω cm^2]	Q [Ω^{-1} cm^2 s^n]	n	R_{film} [Ω cm^2]	W_{ss} [Ω cm^2]	C [μF cm^{-2}]	R_{ct} [Ω cm^2]
CdS nanorods	25.86	2.36×10^{-5}	0.927	2.77×10^{4}	1.53×10^{-5}	9.43×10^{-5}	11.43
$CdS/NiWO_4$ (30%)	23.99	8.24×10^{-5}	0.854	2785	1.01×10^{-5}	3.2×10^{-3}	1.74

field formed between $NiWO_4$ and CdS nanorods enhances the separation of electrons and holes, thereby effectively suppressing charge recombination.

3.5 Potential reaction mechanism

When $NiWO_4$ is combined with CdS nanorods, it will cause the change of the energy level potential, thereby establishing a new interface electric field. The Mott–Schottky method test is based on the function of capacitance and scanning potential. Fig. 10 shows the Mott–Schottky curves of CdS nanorods and $NiWO_4$ photoelectrodes. Their flat band potential can be determined by eqn (7):

$$1/C^2 = 2\left(N_D e \varepsilon \varepsilon_0\right)^{-1} \cdot \left(E - E_{fb} - \kappa T/e\right) \quad (7)$$

C – the capacitance of the space charge region;
N_D – charge carrier concentration;
e – electron charge;
ε_0 – vacuum permittivity;
ε – dielectric constant of CdS and $NiWO_4$;
E – electrode applied potential;
E_{fb} – flat band potential;
T – absolute temperature;
κ – Boltzmann constant;

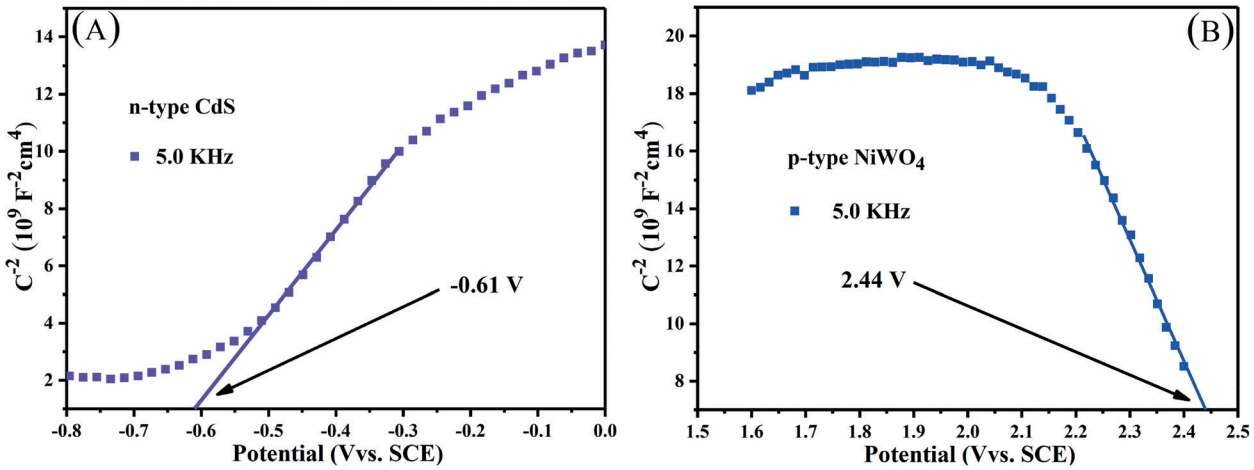

Fig. 10 Mott–Schottky plots of (A) n-type CdS nanorods and (B) p-type $NiWO_4$ at a frequency of 5.0 kHz.

Along the linear portion of the Mott–Schottky curves of CdS nanorods and $NiWO_4$, the tangent is extended to the abscissa. We can not only see that the flat-band potential of CdS nanorods and $NiWO_4$ is −0.61 and 2.44 V *versus* SCE, respectively, but also see that CdS nanorods and $NiWO_4$ are an n-type semiconductor with a positive slope and a p-type semiconductor with a negative slope, respectively.[55] Generally speaking, for an n-type semiconductor, the E_{CB} is more negative by about −0.1 or −0.2 V than the E_{fb}; for a p-type semiconductor, the E_{VB} is more positive by approximately 0.1 or 0.2V than the E_{fb}.[55,56] Therefore, the E_{CB} of CdS nanorods and E_{VB} of $NiWO_4$ are sketchily calculated to be −0.81 and 2.64 V *vs.* SCE. Based on the formula: $E_{NHE} = E_{SCE} + 0.241$, the E_{CB} of CdS nanorods and E_{VB} of $NiWO_4$ are calculated to be −0.569 and 2.881 V *vs.* NHE.

The p–n heterojunction formed between $NiWO_4$ and CdS nanorods is of great importance in promoting the separation of electrons and holes. The Mulliken electronegativity theory (eqn (8) and (9))[36,57] is used to estimate the VB and CB band positions of $NiWO_4$ and CdS nanorods so that we can thoroughly understand the formation of the p-$NiWO_4$/n-CdS heterojunction and the energy band structure.

$$E_{VB} = \chi - E^e + 0.5E_g \quad (8)$$

$$E_{CB} = E_{VB} - E_g \quad (9)$$

where χ is the absolute electronegativity of the semiconductor, which is the geometric mean of the electronegativity of the constituent atoms. The E_g of $NiWO_4$ and CdS is given in Fig. 6(B), and is 2.26 and 2.32 eV, respectively. The χ values of $NiWO_4$ and CdS are determined to be 6.301 (ref. 58) and 5.075 eV,[36] respectively. E^e is the energy of free electrons on the hydrogen scale (4.5 eV *vs.* NHE). Table 4 lists the calculated band positions according to the above formula and relevant data. Through comparison and analysis, the band positions obtained from the Mott–Schottky plot results are close to the calculated ones in Table 4.

Through the above analysis results, we have drawn the energy band position diagram. Fig. 11 shows the band positions of p-$NiWO_4$ and n-CdS before and after contact. At the same time, Fig. 11 and Scheme 1 describe the charge migration process and the photocatalytic reaction process. As a p-type semiconductor, $NiWO_4$'s VB position is more positive and its Fermi level is close to the VB position. However, CdS nanorods are an n-type semiconductor; CdS nanorods' CB position is more negative and its Fermi level is close to the CB position. When $NiWO_4$ is loaded on CdS nanorods, the Fermi level potential of CdS is more negative than the negative potential of $NiWO_4$, which provides a thermodynamic path to promote charge transfer, making the electrons diffuse from the CB of CdS to the CB of $NiWO_4$, resulting in negative charge accumulation in $NiWO_4$. At the same time, holes migrate from the VB of $NiWO_4$ to the VB of CdS nanorods, resulting in the accumulation of positive charges in the CdS nanorods until their Fermi levels are equal. During the Fermi level shifting, the energy bands of the $NiWO_4$ and CdS nanorods move up and down as the Fermi level moves until the two Fermi levels reach equilibrium. Finally, at equilibrium, an internal electric field from the CdS to $NiWO_4$ direction is established at the interface between $NiWO_4$ and CdS nanorods. Under visible light irradiation, CdS and $NiWO_4$ can be excited to generate electrons and holes. Subsequently, under the action of the potential difference and the internal electric field, electrons can

Table 4 The absolute electronegativity, band gap energy, and valence and conduction band edge potential of CdS and $NiWO_4$

Semiconductor	Absolute electronegativity (χ)	Band energy E_g (eV)	Valence band E_{VB} (eV)	Conduction band E_{CB} (eV)
CdS (n-type)	5.075	2.32	1.74	−0.58
$NiWO_4$ (p-type)	6.301	2.26	2.93	0.67

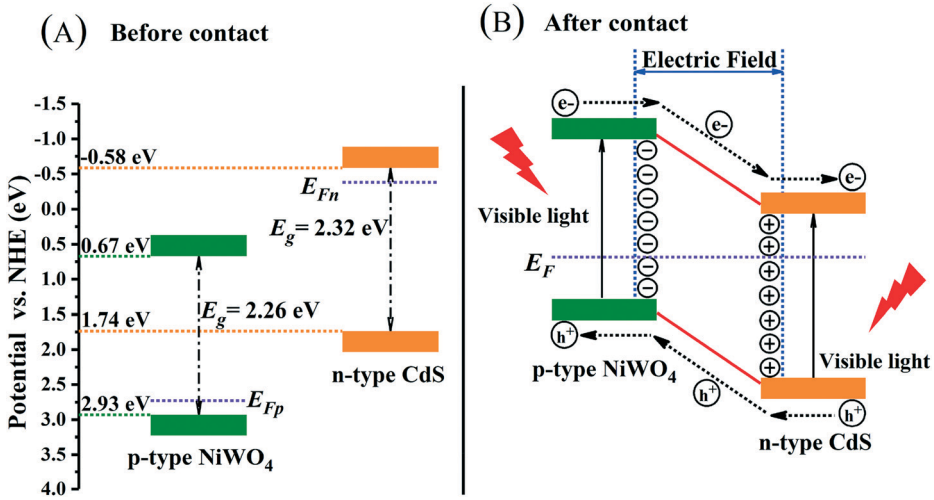

Fig. 11 Schematic diagrams for energy bands of p-$NiWO_4$ and n-CdS (A) before contact and (B) after the formation of the p–n heterojunction.

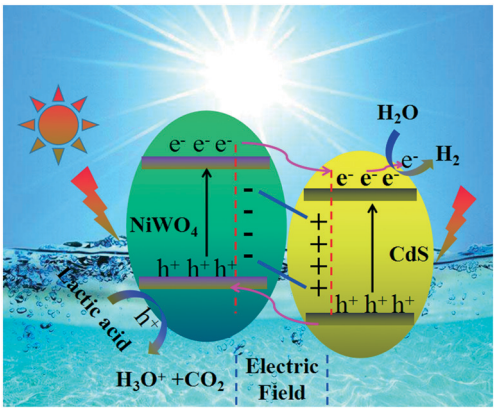

Scheme 1 Photocatalytic mechanism of the CdS/$NiWO_4$ system.

be rapidly transferred from the CB of $NiWO_4$ to the CB of the CdS nanorods, and further migrated to the surface of the CdS nanorods to participate in the reduction of protons to produce H_2. At the same time, photogenerated holes migrate from the VB of CdS nanorods to the VB of $NiWO_4$, further migrate to the surface of $NiWO_4$, and then oxidize lactic acid to produce CO_2 and H_3O^+, thereby effectively promoting the separation of electrons and holes, and improving the photocatalytic H_2 production efficiency of the composite catalyst.

4. Conclusions

In conclusion, a highly-efficient CdS/$NiWO_4$ p–n heterojunction composite catalyst is successfully constructed. In the composite catalyst, the introduction of $NiWO_4$ simultaneously improves the photocatalytic H_2 production performance of CdS nanorods and the stability of photocatalytic H_2 production. The photocatalytic H_2 production properties of the CdS/$NiWO_4$ composite catalyst are closely related to the loading capacity of $NiWO_4$. The [CdS/$NiWO_4$ (30%)] sample has the best H_2 production performance. Under visible light irradiation, the maximum H_2 production in 5 hours is 757 μmol, which is 7.35 times higher than that of pure CdS nanorods. Further studies of photoluminescence spectra, photoelectrochemistry experimental results and Mott–Schottky curves show that the modification of $NiWO_4$ enhances the electron mobility and charge transfer ability of the composite catalyst. However, excessive $NiWO_4$ will reduce the light absorption intensity of CdS nanorods, thereby reducing the hydrogen production activity. It is the built-in electric field formed between $NiWO_4$ and CdS nanorods that accelerates the separation of photogenerated electrons and holes. At the same time, the photogenerated holes on the VB of CdS nanorods can be quickly transferred to the surface of $NiWO_4$, which slows down the photo-corrosion of CdS.

Author contributions

Yongke Zhang and Zhiliang Jin conceived and designed the experiments; Yongke Zhang performed the experiments; Zhiliang Jin contributed reagents/materials and analysis tools; and Yongke Zhang wrote the paper.

Conflicts of interest

The authors declare that they have no competing interests.

Acknowledgements

This work was financially supported by the Chinese National Natural Science Foundation (21862002 and 41663012), the innovation project (YCX18082), North Minzu University, the new technology and system for clean energy catalytic production, and the major scientific project of North Minzu University (ZDZX201803).

References

1 X. P. Tao, Y. Zhao, L. C. Mu, S. Y. Wang, R. G. Li and C. Li, Bismuth Tantalum Oxyhalogen: A Promising Candidate Photocatalyst for Solar Water Splitting, *Adv. Energy Mater.*, 2017, 1701392.

2 J. Low, J. Yu, M. Jaroniec, S. Wageh and A. A. Al-Ghamdi, Heterojunction Photocatalysts, *Adv. Mater.*, 2017, **29**, 1601694.

3 X. Q. Hao, Y. C. Wang, J. Zhou, Z. W. Cui, Y. Wang and Z. G. Zou, Zinc vacancy-promoted photocatalytic activity and photostability of ZnS for efficient visible-light-driven hydrogen evolution, *Appl. Catal., B*, 2018, **221**, 302–311.

4 X. Hai, W. Zhou, K. Chang, H. Pang, H. M. Liu, L. Shi, F. Ichihara and J. H. Ye, Engineering Crystallinity of MoS_2 Monolayers for Highly Efficient Solar Hydrogen Production, *J. Mater. Chem. A*, 2017, **5**, 8591–8598.

5 X. T. Zheng, W. L. Chen, L. Chen, Y. J. Wang, X. W. Guo, J. B. Wang and E. B. Wang, A Strategy for Breaking Polyoxometalate-based MOFs To Obtain High Loading Amounts of Nanosized Polyoxometalate Clusters to Improve the Performance of Dye-sensitized Solar Cells, *Chem. – Eur. J.*, 2017, **23**, 8871–8878.

6 H. Wang, X. Lang, R. Hao, L. Guo, J. Li, L. Wang and X. Han, Facet-Defined AgCl Nanocrystals with Surface-Electronic-StructureDominated Photoreactivities, *Nano Energy*, 2016, **19**, 8–16.

7 X. Chen, S. Shen, L. Guo and S. S. Mao, Semiconductor-Based Photocatalytic Hydrogen Generation, *Chem. Rev.*, 2010, **110**, 6503–6570.

8 Z. C. Guan, H. P. Wang, X. Wang, J. Hu and R. G. Du, Fabrication of heterostructured β-Bi_2O_3-TiO_2 nanotube array composite film for photoelectrochemical cathodic protection applications, *Corros. Sci.*, 2018, **136**, 60–69.

9 H. Q. Xu, J. Hu, D. Wang, Z. Li, Q. Zhang, Y. Luo, S. H. Yu and H. L. Jiang, Visible-Light Photoreduction of CO_2 in a Metal-Organic Framework: Boosting Electron-Hole Separation via Electron Trap States, *J. Am. Chem. Soc.*, 2015, **137**, 13440–13443.

10 X. G. Meng, S. X. Ouyang, T. Kako, P. Li, Q. Yu, T. Wang and J. H. Ye, Photocatalytic CO_2 conversion over alkali modified TiO_2 without loading noble metal cocatalyst, *Chem. Commun.*, 2014, **50**, 11517.

11 A. Fujishima and K. Honda, Electrochemical Photolysis of Water at a Semiconductor Electrode, *Nature*, 1972, **238**, 37–38.

12 X. Bai, L. Wang, R. Zong, Y. Lv, Y. Sun and Y. Zhu, Performance Enhancement of ZnO Photocatalyst via Synergic Effect of Surface Oxygen Defect and Graphene Hybridization, *Langmuir*, 2013, **29**, 3097–3105.

13 Q. Li, B. D. Guo, J. G. Yu, J. R. Ran, B. H. Zhang, H. J. Yan and J. R. Gong, Highly Efficient Visible-Light-Driven Photocatalytic Hydrogen Production of CdS-Cluster-Decorated Graphene Nanosheets, *J. Am. Chem. Soc.*, 2011, **133**, 10878–10884.

14 X. Wu, H. B. Zhang, J. C. Dong, M. Qiu, J. T. Kong, Y. F. Zhang, Y. Li, G. L. Xu, J. Zhang and J. H. Ye, Surface Step Decoration of Isolated Atom as Electron Pumping: AtomicLevel Insights into Visible-Light Hydrogen Evolution, *Nano Energy*, 2018, **45**, 109–117.

15 B. B. Zhang, G. J. Dong, L. Wang, Y. J. Zhang, Y. Ding and Y. P. Bi, Efficient hydrogen production from MIL-53(Fe) catalyst-modified Mo: BiVO4 photoelectrodes, *Catal. Sci. Technol.*, 2017, **7**, 4971.

16 G. C. Xi and J. H. Ye, Synthesis of bismuth vanadate nanoplates with exposed {001} facets and enhanced visible-light photocatalytic properties, *Chem. Commun.*, 2010, **46**, 1893–1895.

17 Y. P. Bi, H. Y. Hu, S. X. Ouyang, Z. B. Jiao, G. X. Lu and J. H. Ye, Selective Growth of Metallic Ag Nanocrystals on Ag_3PO_4 Submicro-Cubes for Photocatalytic Applications, *Chem. – Eur. J.*, 2012, **18**, 14272.

18 K. Leistner, K. Duschek, J. Zehner, M. Yang, A. Petr, K. Nielsch and K. L. Kavanagh, Role of Hydrogen Evolution during Epitaxial Electrodeposition of Fe on GaAs, *J. Electrochem. Soc.*, 2018, **165**(4), H3076–H3079.

19 Z. W. Ren, J. K. Sun, H. Li, P. Mao, Y. Z. Wei, X. H. Zhong, J. S. Hu, S. Y. Yang and J. Z. Wang, Bilayer PbS Quantum Dots for High-Performance Photodetectors, *Adv. Mater.*, 2017, 1702055.

20 L. Zhang, H. B. Wu, S. Madhavi, H. H. Hng and X. W. Lou, Formation of Fe_2O_3 Microboxes with Hierarchical Shell Structures from Metal-Organic Frameworks and Their Lithium Storage Properties, *J. Am. Chem. Soc.*, 2012, **134**(42), 17388–17391.

21 B. B. Liu, X. J. Liu, M. Y. Ni, C. J. Feng, X. Lei, C. Li, Y. Y. Gong, L. Y. Niu, J. L. Li and L. K. Pan, SnO_2 as co-catalyst for enhanced visible light photocatalytic activity of Bi_2MoO_6, *Appl. Surf. Sci.*, 2018, **453**, 280–287.

22 T. P. Hu, P. F. Li, J. F. Zhang, C. H. Liang and K. Dai, Highly efficient direct Z-scheme WO_3/CdS-diethylenetriamine photocatalyst and its enhanced photocatalytic H_2 evolution under visible light irradiation, *Appl. Surf. Sci.*, 2018, **442**, 20–29.

23 Q. Y. Li, T. Kako and J. H. Ye, WO_3 modified titanate network film: highly efficient photo-mineralization of 2-propanol under visible light irradiation, *Chem. Commun.*, 2010, **46**, 5352–5354.

24 M. G. Walter, E. L. Warren, J. R. McKone, S. W. Boettcher, Q. Mi, E. A. Santori and N. S. Lewis, Solar Water Splitting Cells, *Chem. Rev.*, 2010, **110**(11), 6446–6473.

25 Y. Y. Bu, Z. Y. Chen, W. B. Li and B. R. Hou, Highly Efficient Photocatalytic Performance of Graphene-ZnO Quasi-ShellCore Composite Material, *ACS Appl. Mater. Interfaces*, 2013, **5**(23), 12361–12368.

26 Z. Zhang and J. T. Yates Jr, Band Bending in Semiconductors: Chemical and Physical Consequences at Surfaces and Interfaces, *Chem. Rev.*, 2012, **112**(10), 5520–5551.

27 W. L. Zhen, X. F. Ning, B. J. Yang, Y. Q. Wu, Z. Li and G. X. Lu, The enhancement of CdS photocatalytic activity for water splitting via antiphotocorrosion by coating Ni_2P shell and removing nascent formed oxygen with artificial gill, *Appl. Catal., B*, 2018, **221**, 243–257.

28 J. Y. Zhang, Y. H. Wang, J. Jin, J. Zhang, Z. Lin, F. Huang and J. G. Yu, Efficient Visible-Light Photocatalytic Hydrogen

Evolution and Enhanced Photostability of Core/Shell CdS/g-C_3N_4 Nanowires, *ACS Appl. Mater. Interfaces*, 2013, **5**, 10317–10324.

29 M. Y. Xing, B. C. Qiu, M. M. Du, Q. H. Zhu, L. Z. Wang and J. L. Zhang, Spatially Separated CdS Shells Exposed with Reduction Surfaces for Enhancing Photocatalytic Hydrogen Evolution, *Adv. Funct. Mater.*, 2017, **27**, 1702624.

30 M. G. Wang, H. Zhang, H. L. Zu, Z. R. Zhang and J. Han, Construction of TiO_2/CdS heterojunction photocatalysts with enhanced visible light activity, *Appl. Surf. Sci.*, 2018, **455**, 729–735.

31 Q. Liang, S. N. Cui, C. H. Liu, S. Xu, C. Yao and Z. Y. Li, Construction of CdS@UIO-66-NH_2 core-shell nanorods for enhanced photocatalytic activity with excellent photostability, *J. Colloid Interface Sci.*, 2018, **524**, 379–387.

32 C. Feng, Z. Y. Chen, J. Hou, J. R. Li, X. B. Li, L. K. Xu, M. X. Sun and R. C. Zeng, Effectively enhanced photocatalytic hydrogen production performance of one-pot synthesized MoS_2 clusters/CdS nanorod heterojunction material under visible light, *Chem. Eng. J.*, 2018, **345**, 404–413.

33 Y. J. Zou, J. W. Shi, D. D. Ma, Z. Y. Fan, L. H. Cheng, D. K. Sun, Z. Y. Wang and C. M. Niu, WS_2/Graphitic Carbon Nitride Heterojunction Nanosheets Decorated with CdS Quantum Dots for Photocatalytic Hydrogen Production, *ChemSusChem*, 2018, **11**, 1187–1197.

34 D. D. Zheng, G. G. Zhang and X. C. Wang, Integrating CdS quantum dots on hollow graphitic carbon nitride nanospheres for hydrogen evolution photocatalysis, *Appl. Catal., B*, 2015, **179**, 479–488.

35 H. M. Wang, C. H. Li, L. Ying and P. F. Fang, WO_3&WS_2 nanorods coupled with CdS nanoparticles for enhanced visible light driven hydrogen evolution, *Appl. Surf. Sci.*, 2018, **448**, 539–546.

36 Y. L. Han, Z. B. Liang, H. F. Dang and X. F. Dong, Extremely high photocatalytic H_2 evolution of novel Co_3O_4/$Cd_{0.9}Zn_{0.1}S$ p-n heterojunction photocatalyst under visible light irradiation, *J. Taiwan Inst. Chem. Eng.*, 2018, 1–8.

37 M. M. Mohamed, S. A. Ahmed and K. S. Khairou, Unprecedented high photocatalytic activity of nanocrystalline WO_3/$NiWO_4$ hetero-junction towards dye degradation: Effect of template and synthesis conditions, *Appl. Catal., B*, 2014, **150–151**, 63–73.

38 M. Pirhashemi and A. H. Yangjeh, ZnO/$NiWO_4$/Ag_2CrO_4 nanocomposites with p-n-n heterojunctions: highly improved activity for degradations of water contaminants under visible light, *Sep. Purif. Technol.*, 2018, **193**, 69–80.

39 T. H. Do, C. N. Van, K. A. Tsai, L. T. Quynh, J. W. Chen, Y. C. Lin, Y. C. Chen, W. C. Chou, C. L. Wu, Y. J. Hsu and Y. H. Chu, Superior photoelectrochemical activity of self-assembled $NiWO_4$-WO_3 heteroepitaxy, *Nano Energy*, 2016, **23**, 153–160.

40 H. Y. Aziz and S. G. Maryam, Novel magnetic Fe_3O_4/ZnO/$NiWO_4$ nanocomposites: Enhanced visible-light photocatalytic performance through p-n heterojunctions, *Sep. Purif. Technol.*, 2017, **184**, 334–346.

41 Y. K. Zhang, Z. L. Jin, H. Yuan, G. R. Wang and B. Z. Ma, Well-regulated nickel nanoparticles functional modified ZIF-67(Co) derived Co_3O_4/CdS p-n heterojunction for efficient photocatalytic hydrogen evolution, *Appl. Surf. Sci.*, 2018, **462**, 213–225.

42 Y. K. Zhang, G. R. Wang, W. Ma, B. Z. Maa and Z. L. Jin, CdS p-n heterojunction co-boosting with Co_3O_4 and Ni-MOF-74 for photocatalytic hydrogen evolution, *Dalton Trans.*, 2018, **47**, 11176.

43 S. M. Chen, G. Yang, Y. Jia and H. J. Zheng, Three-dimensional $NiCo_2O_4$@$NiWO_4$ core-shell nanowire arrays for high performance supercapacitors, *J. Mater. Chem. A*, 2017, **5**, 1028.

44 D. Kumar, S. Hong, D. Reddy and T. Kim, Ultrathin MoS_2 layers anchored exfoliated reduced graphene oxide nanosheet hybrid as a highly efficient cocatalyst for CdS nanorods towards enhanced photocatalytic hydrogen production, *Appl. Catal., B*, 2017, **212**, 7–14.

45 A. Y. Meng, B. C. Zhu, B. Zhong, L. Y. Zhang and B. Cheng, Direct Z-scheme TiO_2/CdS hierarchical photocatalyst for enhanced photocatalytic H_2-production activity, *Appl. Surf. Sci.*, 2017, **422**, 518–527.

46 P. Ye, X. L. Liu, J. Iocozzia, Y. P. Yuan, L. N. Gu, G. S. Xu and Z. Q. Lin, A highly stable non-noble metal Ni_2P co-catalyst for increased H_2 generation by g-C_3N_4 under visible light irradiation, *J. Mater. Chem. A*, 2017, **5**, 8493–8498.

47 J. Zhu, W. Z. Li, J. Li, Y. M. Li, H. S. Hu and Y. H. Yang, Photoelectrochemical activity of $NiWO_4$/WO_3 heterojunction photoanode under visible light irradiation, *Electrochim. Acta*, 2013, **112**, 191–198.

48 M. M. Mohamed, M. Khairy and S. Eid, Polyethylene glycol assisted one-pot hydrothermal synthesis of $NiWO_4$/WO_3 heterojunction for direct Methanol fuel cells, *Electrochim. Acta*, 2018, **263**, 286–298.

49 A. Kalinko, A. Kotlov, A. Kuzmin, V. Pankratov, A. I. Popov and L. Shirmane, Electronic excitations in $ZnWO_4$ and $Zn_xNi_{1-X}WO_4$ (x=0.1-0.9) using VUV synchrotron radiation, *Cent. Eur. J. Phys.*, 2011, **9**, 432–437.

50 A. L. M. De Oliveira and I. M. G. Dos Santos, Yellow $Zn_xNi_{1-x}WO_4$ pigments obtained using a polymeric precursor method, *Dyes Pigm.*, 2008, **77**, 210–217.

51 Z. D. Lou, J. H. Hao and M. Cocivera, Luminescence of $ZnWO_4$ and $CdWO_4$ thin films prepared by spray pyrolysis, *J. Lumin.*, 2002, **99**, 349–453.

52 Z. Y. Zhang, J. D. Huang, M. Y. Zhang, Q. Yuan and B. Dong, Ultrathin hexagonal SnS_2 nanosheets coupled with g-C_3N_4 nanosheets as 2D/2D heterojunction photocatalysts toward high photocatalytic activity, *Appl. Catal., B*, 2015, **163**, 298–305.

53 X. W. Shi, M. Fujitsuka, S. Kim and T. Majima, Faster Electron Injection and More Active Sites for Efficient Photocatalytic H_2 Evolution in g-C_3N_4/MoS_2 Hybrid, *Small*, 2018, **14**, 1703277.

54 S. Q. Peng, X. P. Zeng and Y. X. Li, Titanate nanotube modified with different nickel precursors for enhanced Eosin Y-sensitized photocatalytic hydrogen evolution, *Int. J. Hydrogen Energy*, 2015, **40**, 6038–6049.

55 F. Guo, W. Shi, H. Wang, M. Han, H. Li, H. Huang, Y. Liu and Z. Kang, Facile fabrication of a CoO/g-C_3N_4 p-n heterojunction with enhanced photocatalytic activity and stability

for tetracycline degradation under visible light, *Catal. Sci. Technol.*, 2017, **7**, 3325–3331.

56 X. Li, J. Yu, J. Low, Y. Fang, J. Xiao and X. Chen, Engineering heterogeneous semiconductors for solar water splitting, *J. Mater. Chem. A*, 2015, **3**, 2485–2534.

57 X. Hao, Z. Jin, H. Yang, G. Lu and Y. Bi, Peculiar synergetic effect of MoS_2 quantum dots and graphene on Metal-Organic Frameworks for photocatalytic hydrogen evolution, *Appl. Catal., B*, 2017, **210**, 45–56.

58 M. Pirhashemi and A. Habibi-Yangjeh, $ZnO/NiWO_4/Ag_2CrO_4$ nanocomposites with p-n-n heterojunctions: highly improved activity for degradations of water contaminants under visible light, *Sep. Purif. Technol.*, 2018, **193**, 69–80.

